

# DUCPS: Deep Unfolding the Cauchy Proximal Splitting Algorithm for B-Lines Quantification in Lung Ultrasound Images

Tianqi Yang, Oktay Karakuş, *Member, IEEE*, Nantheera Anantrasirichai, *Member, IEEE*, Marco Allinovi and Alin Achim, *Senior Member, IEEE*

## Abstract

The identification of artefacts, particularly B-lines, in lung ultrasound (LUS), is crucial for assisting clinical diagnosis, prompting the development of innovative methodologies. While the Cauchy proximal splitting (CPS) algorithm has demonstrated effective performance in B-line detection, the process is slow and has limited generalization. This paper addresses these issues with a novel unsupervised deep unfolding network structure (DUCPS). The framework utilizes deep unfolding procedures to merge traditional model-based techniques with deep learning approaches. By unfolding the CPS algorithm into a deep network, DUCPS enables the parameters in the optimization algorithm to be learnable, thus enhancing generalization performance and facilitating rapid convergence. We conducted entirely unsupervised training using the Neighbor2Neighbor (N2N) and the Structural Similarity Index Measure (SSIM) losses. When combined with an improved line identification method proposed in this paper, state-of-the-art performance is achieved, with the recall and F2 score reaching 0.70 and 0.64, respectively. Notably, DUCPS significantly improves computational efficiency eliminating the need for extensive data labeling, representing a notable advancement over both traditional algorithms and existing deep learning approaches.

## Index Terms

Deep unfolding, Cauchy proximal splitting, lung ultrasound, line detection, inverse problem

## I. INTRODUCTION

Lung ultrasound (LUS) has emerged as a highly effective diagnostic tool for a wide range of pulmonary conditions. Over recent years, there has been a significant advancement in techniques for analyzing lung ultrasound images, rendering it an invaluable asset in medical diagnostics [1]. One of the key features in LUS are the so-called B-lines, which manifest as laser-like, vertical, hyperechoic reverberation artifacts originating from the pleural line [2].

Tianqi Yang, Nantheera Anantrasirichai and Alin Achim are with Visual Information Laboratory, University of Bristol, Bristol, BS8 1UB UK (e-mail: tianqi.yang@bristol.ac.uk; n.anantrasirichai@bristol.ac.uk; alin.achim@bristol.ac.uk).

Oktay Karakuş is with School of Computer Science and Informatics, Cardiff University, Cardiff, CF24 4AG UK (e-mail: KarakuşO@cardiff.ac.uk).

Marco Allinovi is with Nephrology, Dialysis and Transplantation, Careggi University Hospital, Florence, Italy (e-mail: marco.allinovi@gmail.com).

The motivation behind research into B-line detection is multifaceted. Firstly, the accurate identification and quantification of B-lines can significantly improve the early diagnosis and management of various lung conditions, reducing the need for more invasive procedures like CT scans or bronchoscopy, which are often more expensive and less readily available. Early and precise detection of pulmonary issues through B-lines can lead to timely and targeted therapeutic interventions, potentially reducing morbidity and mortality associated with diseases such as pneumonia and pulmonary edema. Studies have demonstrated their correlation with the volume of extravascular lung water [3]–[5]. Moreover, enhancing the automated detection of B-lines through advanced imaging algorithms holds the promise of making LUS more accessible and easier to use for clinicians who may not have specialized training in ultrasound imaging. This democratization of lung ultrasound technology can be particularly beneficial in resource-limited settings or during large-scale health crises, such as the COVID-19 pandemic, where rapid and widespread pulmonary assessment is crucial. Additionally, understanding the nuances of B-line formation and their exact correlation with different pathological states can deepen our overall knowledge of pulmonary physiology and pathophysiology. For instance, in chronic kidney disease, fluid overload and pulmonary congestion are common complications that can be effectively monitored through B-line detection, providing critical insights for managing such patients and preventing further complications. This, in turn, can inspire the development of new therapeutic approaches and preventive measures for lung-related illnesses. In essence, the ongoing research and development in B-line detection aim not only to enhance diagnostic accuracy and efficiency but also to broaden the applicability of LUS, ensuring that more patients benefit from this powerful diagnostic tool across various healthcare settings.

Various techniques have been utilized in previous endeavors to automatically detect B-lines. Brattain et al. [6] employed hand-crafted image processing techniques such as polar reformatting and thresholding. Moshavegh et al. [7] employed a random walk method to delineate the pleural line and then applied an alternate sequential filtration to identify B-lines, excluding the upper pleural region. Anantrasirichai et al. [8], [9] proposed line detection as an inverse problem, wherein a B-mode LUS image is transformed into a representation of radius and orientation in the Radon domain. Subsequently, they solved the inverse problem using the alternating direction method of multipliers (ADMM) [10]. Farahi et al. [11] then developed an algorithm based on the use of Wavelet to denoise and Radon transforms to extract LUS features. Further contributions to model-based methods were later proposed by Karakus et al. [12] for assessing COVID-19 patients, achieving improved performance by regularizing the solution with the Cauchy proximal splitting (CPS) algorithm [13]. While model-based methods do not rely on learning mappings from data directly, data is often employed to estimate a small number of parameters. However, simplistic models frequently struggle to capture the nuances of high-dimensional complex data and dynamic variations.

With the emergence of deep learning, convolutional neural networks (CNNs) have become key in robust B-line detection. CNNs can learn complex mappings that are difficult to manually design. Van Sloun and Demi [14] used a CNN with gradient-based class activation mapping (Grad-CAM) [15] to detect B-lines in LUS frames. Roy et al. [16] expanded on this with a spatial transformer network (STN) for weakly supervised localization of pathological patterns and scoring COVID-19 severity. Improved performance was obtained by adding domain knowledge into deep neural networks [17]. Mason et al. achieved better segmentation performance through domain adaptation, exploring B-line segmentation in LUS frames of COVID-19 and pneumonia patients. Several methodologies utilize

both spatial and temporal information, including the use of 3-D filters [18] and spatio-temporal attention [19]. To address the challenge of obtaining expert annotations, Zhao et al. [20] used simulated LUS images to train CNNs for B-line artifact segmentation, while our previous study [21] explored contrastive learning for unsupervised B-line representation.

The limitations present in model-based methods and opaque deep learning systems have prompted the emergence of integrated techniques. These techniques aim to mitigate the drawbacks of each approach while capitalizing on their respective strengths. Model-based techniques often struggle with capturing complex patterns and may require extensive domain knowledge for accurate modeling, while deep learning systems lack interpretability and can be challenging to implement without labeled data. Merging these techniques combines the robustness and interpretability of traditional signal processing with the flexibility of deep learning, yielding a more comprehensive approach. This integration enhances performance, facilitates better analysis, and improves understanding of underlying data for specific tasks. In the influential study by Gregor and LeCun [22], a promising approach known as algorithm unfolding (or unrolling) was introduced, facilitating the linkage of iterative algorithms like sparse coding techniques with neural networks. This research has inspired further studies in different areas of biomedical research, such as compressive sensing [23], computed tomography [24], [25], and ultrasonography [26].

In this work, we propose a novel framework for B-line detection that leverages the advantages of model-based methods, eliminating the need for labeled data, and the fast inference capabilities of deep learning to enable real-time operation. This extends our previous work [27], where we adopt deep unfolding to achieve rapid convergence by training a feedforward neural network to approximate iterative algorithms. Here, we model the lines in noisy LUS images via a Radon transform and reconstruct the lines employing the Cauchy prior. Then, we unfold the CPS algorithm for solving the inverse problem for line detection in LUS images, aiming to address a drawback inherent in its manually predefined parameter configuration, which may limit its ability to generalize effectively. The architecture of the deep unfolded CPS (DUCPS) algorithm is shown in Fig.1. A morphological line identification procedure is subsequently used to localize horizontal (pleural line and A-lines) and vertical (B-lines) line artifacts. The proposed method outpaces traditional model-based methods by a significant margin, boasting speeds up to 10 times faster than PUI [9]. In comparison to state-of-the-art neural network detection, it demonstrates reproducibility and explainability, making it ideal for real-time B-line detection.

To summarize, the main contributions of this work are:

- 1) We propose an unsupervised deep unfolding network structure (DUCPS) designed to solve the inverse problem of model-based line detection in LUS images. Specifically, we unfold the Cauchy proximal splitting (CPS) algorithm into a deep network, enabling the parameters in the optimization algorithm to be learnable.
- 2) We train the network with the Neighbor2Neighbor loss, considering its effectiveness in handling noisy images. This approach significantly improves precision, recall, and F-scores compared to DUBLINE [27];
- 3) We introduce a morphological approach to identify B-lines in LUS images by restricting the search area and detecting local maxima in the Radon domain, thereby distinguishing B-lines from other line artifacts efficiently.
- 4) We design a scoring method to evaluate B-line detection accuracy, which offers precise feedback on detection

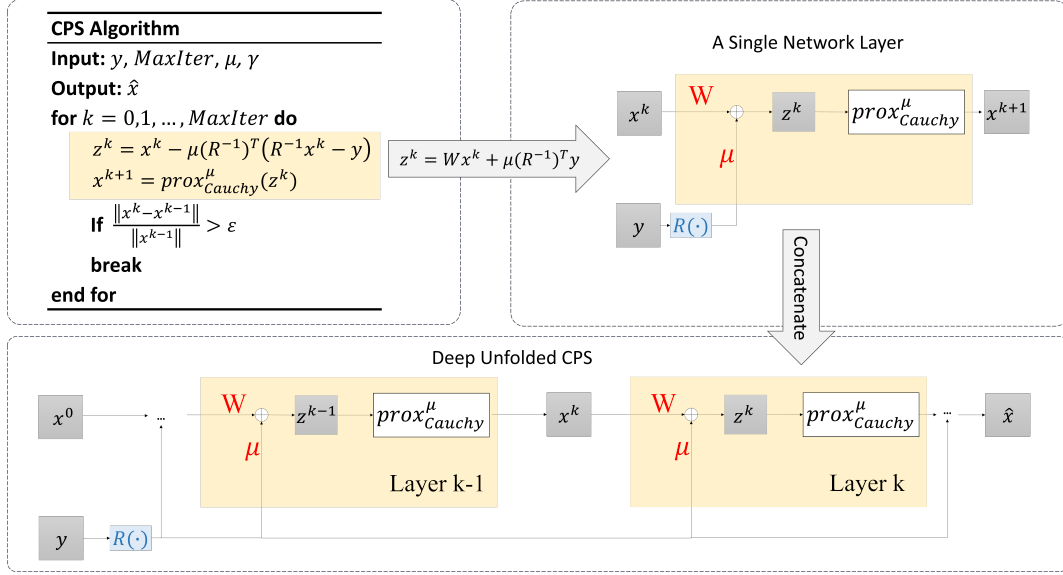


Fig. 1. Diagrammatic representation of DUCPS. The iteration step (yellow block) is executed a number of times corresponding to the network layers. Each iteration  $k$  depends on algorithm parameters, which are transferred into network parameters  $W$  and  $\mu$  (coloured in red) which are learned from training datasets through end-to-end training.

positioning relative to the target area.

The remainder of this paper is organized as follows: we present the proposed DUCPS algorithm and the line artifact identification method in detail in Section II. Section III introduces the method designed for evaluating our method. In Section IV, we describe the data used in the study, and show the experimental results as well as the comparison with other methods. Finally, Section V concludes this article with remarks and future work directions.

## II. METHODOLOGY

### A. Line artefact model

An ultrasound image can be represented as the result of applying an inverse Radon transform to a set of lines in a forward model, as

$$y = R^{-1}x + n, \quad (1)$$

where the observed ultrasound image, denoted as  $y$ , corresponds to a set of lines  $x$  characterised by a distance  $r$  from the center of  $y$  and an orientation  $\omega$  from the horizontal axis of the image. Represented by  $R$  and  $R^{-1}$ , the Radon transform and its inverse are involved and are used as in [28], while  $n$  signifies the additive noise. In a noise-free scenario, the Radon transform is typically defined as shown in (2), where  $\delta(\cdot)$  denotes the Dirac-delta function.

$$x = \int_{\mathbb{R}^2} y(i, j) \delta(r - i \cos \omega - j \sin \omega) di dj. \quad (2)$$

The Cauchy distribution is recognized as a distinctive member within the  $\alpha$ -stable distribution family, acknowledged for its heavy-tailed nature and its tendency to encourage sparsity [29], in particular in transform domain



representations of ultrasound images [30]. The closed-form probability density function of the Cauchy distribution is given by

$$p(x) \propto \frac{\gamma}{\gamma^2 + x^2}, \quad (3)$$

where  $\gamma$  serves as the scale (or dispersion) parameter, governing the extent of distribution spread. Therefore, utilizing maximum a posteriori estimation, the reconstruction of  $x$  can be accomplished using the subsequent equation, taking into account the model described in (1) and employing the Cauchy prior.

$$\hat{x} = \arg \min_x \left\{ \frac{\|y - R^{-1}x\|_2^2}{2\sigma^2} - \sum_{i,j} \log \frac{\gamma}{\gamma^2 + x_{i,j}^2} \right\} \quad (4)$$

### B. Deep Unfolded CPS

**Deep Unfolding in Model-Driven Neural Networks:** Deep unfolding is a method that integrates iterative algorithms with neural network techniques to efficiently solve optimization problems [31]. As shown in Fig.1, this approach takes an iterative optimization algorithm with the maximum number of iterations, unfolds its structure, and incorporates trainable parameters. These parameters are then optimized using deep learning techniques including loss functions, optimizers, and backpropagation. The resultant unfolded algorithm, enhanced with learned parameters, can be applied to B-line detection in LUS images.

In more detail, the problem in (4) can be solved by employing the CPS algorithm [12] which computes the proximal operator of the Cauchy-based penalty and employs the forward-backward (FB) algorithm for optimization. By leveraging the well-defined iterative mathematical formulation of CPS, we unfold the algorithm into a neural network architecture. The unfolding process proposed below will allow the network parameters to be trained end-to-end using gradient-based optimization. The inputs to the network are the initial states, including the original image  $y$  in the spatial domain and its corresponding radon transform  $x$ , and the output is the prediction  $\hat{x}$  after a certain number of iterations.

**Neural network formulation:** To unfold CPS, iteration (5) and (6) can be reformulated into a single network layer as depicted in Fig.1. This layer encompasses a sequence of analytical operations, including matrix-vector multiplication, summation, and the Cauchy proximal operator, which are analogous to the operations within a neural network. A diagrammatic representation of one iteration step elucidates its similarity to a single network layer. Executing CPS  $k$  times can be interpreted as cascading  $k$  such layers, thereby forming a  $k$ -layer neural network. In each layer, the optimisation can be broken up into a forward gradient step using the data fidelity term with the form of  $(\|y - R^{-1}x\|_2^2)/2\sigma^2$ , and a backward step using the Cauchy-based penalty. In this way, the trained network corresponds exactly to the original algorithm.

In the forward gradient step, the intermediate variable  $z^k$  is updated by

$$\begin{aligned} z^k &= x^k - \mu(R^{-1})^T(R^{-1}x^k - y), \\ &= Wx^k + \mu(R^{-1})^Ty, \end{aligned} \quad (5)$$

where  $\mu$  refers to the step size, and  $(R^{-1})^T$  serves as the forward Radon projection [32].  $W$  and  $\mu$  are trainable matrices with positive elements.  $W$  is initialized as a constant matrix that has the same size as  $x$ , with elements

nearly equal to 1, while  $\mu$  is set to be a single-element matrix with a value close to 0 so that  $z^0 \approx x^0$ . In this paper, we use  $1 - 10^{-5}$  and  $10^{-5}$  to initialise  $W$  and  $\mu$  respectively. The  $R$  and  $R^{-1}$  are constructed by *Radon\_transformation* functions<sup>1</sup>.

In the backward step,  $x^k$  is updated by

$$x^{k+1} = \text{prox}_{Cauchy}^\mu(z^k) \quad (6)$$

where the Cauchy proximal operator is defined as

$$\text{prox}_{Cauchy}^\mu(z) = \arg \min_u \left\{ \frac{\|z - u\|_2^2}{2\mu} - \log \frac{\gamma}{\gamma^2 + u^2} \right\}. \quad (7)$$

As suggested in [13], obtaining the solution to this minimization problem involves differentiating (7) with respect to  $u$ , and setting the resulting expression to zero. Consequently, we arrive at the cubic function given in (8) and the solution to this function can be obtained through Cardano's method as first shown in [33].

$$u^3 - zu^2 + (\gamma^2 + 2\mu)u - z\gamma^2 = 0 \quad (8)$$

To comply with the CPS algorithm, we set the number of layers to meet the stopping criteria when

$$\frac{\|x^k - x^{k-1}\|}{\|x^{k-1}\|} < 10^{-3}$$

It is noteworthy that the number of layers  $k$  in the trained network can be significantly lower—by an order of magnitude—than the number of iterations needed for the original CPS algorithm to converge for a new input. This substantial reduction markedly enhances optimisation efficiency.

**Loss function:** After unfolding CPS into a network, which we prefer to refer to as DUCPS, the network is trained through back-propagation using real datasets to optimise the parameters  $W$  and  $\mu$ . Considering that we aim to train the network in an unsupervised way, we employ the Neighbor2Neighbor (N2N) training scheme [34] as it can train the network from a single image and is suitable for noisy input. For detailed discussions, we refer the reader to Section 3 and Section 4 of [34]. The training framework is depicted in Fig. 2. A pair of sub-sampled images  $(g_1(y), g_2(y))$  are generated from a neighbor sub-sampler  $G$  [34] to generate noisy image pairs from single noisy images  $Ry$  for training. The loss function includes a reconstruction term  $L_{rec}$ , which is computed between the network output and the noisy target, and a regularisation term  $L_{reg}$  that measures the difference of the ground-truth pixel values between the sub-sampled noisy image pair.

$$\begin{aligned} Loss_{N2N} = L_{rec} + \alpha L_{reg} = & \|f_\theta(g_1(Ry)) - g_2(Ry)\|_2^2 \\ & + \alpha \cdot \|f_\theta(g_1(Ry)) - g_2(Ry) - (g_1(f_\theta(Ry)) - g_2(f_\theta(Ry)))\|_2^2, \end{aligned} \quad (9)$$

where  $f_\theta(\cdot)$  refers to DUCPS with  $\theta$  representing the network parameters.  $\alpha$  is a hyper-parameter that controls the strength of the regularisation term.

We also investigate the algorithm performance when training with a common loss, i.e. the Structural Similarity Index Measure (SSIM) loss, used in computer vision tasks and also in our previous work [27]. We trained the

<sup>1</sup><https://github.com/drgHannah/Radon-Transformation/tree/main>

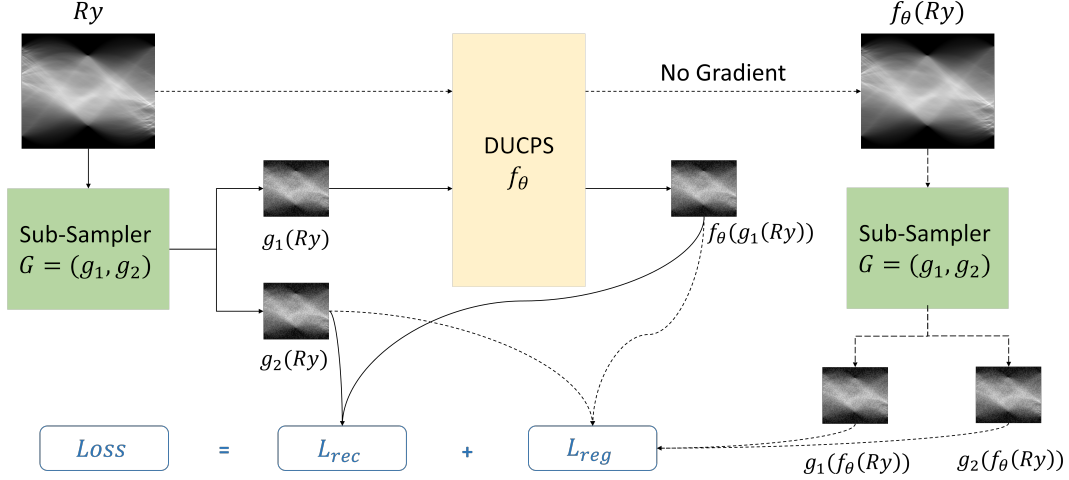


Fig. 2. The overview of Neighbor2Neighbor training scheme [34]. The neighbor sub-samplers that appear twice are the same.

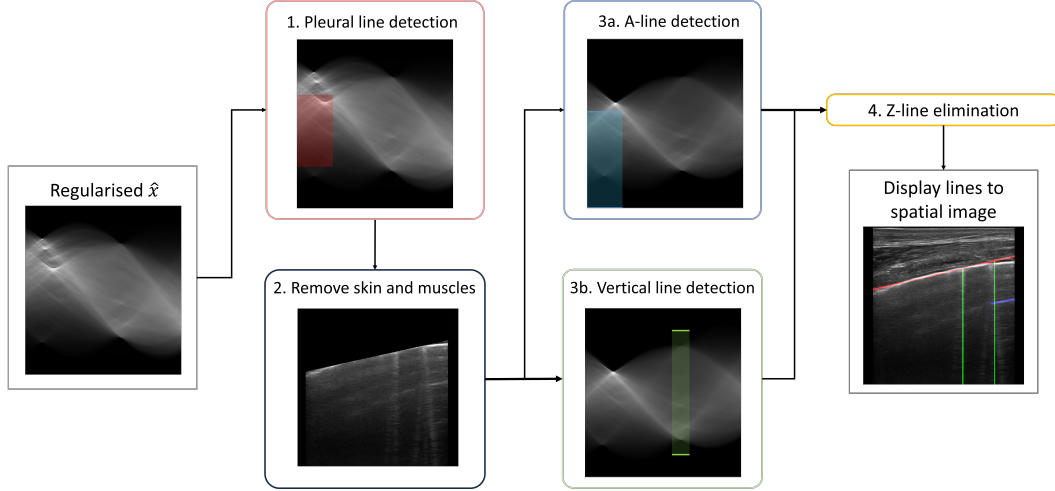


Fig. 3. The process of identifying line artifacts. Searching areas for the pleural line (red), A-line (blue), and B-line (green) are masked in the Radon domain. The detected pleural line is displayed in red, the A-line is in blue, and the B-lines are depicted in green.

network to maximize the SSIM [35] between the intermediate variable  $z^k$  and the input image. Incorporating the forward step in the FB algorithm achieves the purpose of data fitting, thereby defining the loss function as follows:

$$Loss_{SSIM} = (1 - SSIM(R^{-1}(z^k), y)). \quad (10)$$

### C. Line identification

The line identification process is implemented after acquiring the restored image  $\hat{x}$  using the local maxima technique. The steps are illustrated in Fig. 3 and described below.

It is crucial to set different searching areas to distinguish line artefacts considering that they possess characteristic structures in the spatial domain. This includes limiting the searching angles and upper and lower borders in the

Radon domain. For pleural line and A-lines, we limit the searching angle within the range  $\Omega_h \in [90^\circ \pm 20^\circ]$  ( $0^\circ$  originates from the  $x$  axis, which indicates a horizontal line) as they are generally horizontal. Similarly, the B-lines are detected at  $\Omega_v \in [\pm 10^\circ]$ .

**Step 1.** Given an LUS image  $y$  having a height of  $H$  pixels, the borders of pleural line searching are defined as

$$\text{Pleural line upper border} = \frac{1}{3}H, \quad (11)$$

$$\text{Pleural line lower border} = \frac{1}{4}H. \quad (12)$$

This setting accounts for the fact that the pleural line represents the junction of the visceral and parietal pleura, while also helping to mitigate the influence of the appearance of the chest wall and intercostal muscles in the upper area of the image. Then, the provided search area is scanned to detect the local peaks of the reconstructed Radon information. We select the local peak with the maximum intensity as the detected pleural line, as it is typically the brightest line within the corresponding search area in the spatial domain.

**Step 2.** The area above the detected pleural line in the spatial image is removed to facilitate the detection of remaining artifacts. By comparing the Radon images in Step 1 and Step 3, we can observe that the Radon information becomes less noisy after the removal of redundant tissue, revealing clearer local peak information for subsequent steps. The detections will be performed based on the Radon transform of the dimmed image.

**Step 3a.** On the one hand, A-lines are equidistant physiological horizontal lines below the pleural line, and the distance between them is equal to the distance between skin and pleural line. Therefore, the searching area for A-lines are limited as

$$\text{A-line upper border} = \frac{1}{2}H - \frac{3}{2}H_p, \quad (13)$$

$$\text{A-line lower border} = \frac{1}{2}H, \quad (14)$$

where  $H_p$  denotes the distance from the detected pleural line and the center of  $y$ .

On the other hand, as A-lines may appear less distinct or weaker in intensity at greater depths compared to shallower depths in LUS images, we set a threshold to validate the candidate peak points and select the brightest as the detected A-line. The intensity of the validated A-line ( $I_A$ ) should satisfy

$$I_A \geq \lambda I_p, \quad (15)$$

where  $\lambda \in [0, 1]$  is a proportional parameter and  $I_p$  refers to the intensity of the detected pleural line.

**Step 3b.** In the case of using a linear transducer, possible locations of vertical artefacts can span across the entire width ( $W$ ) of the image, and therefore candidate B-lines are detected in the Radon domain within the border

$$\text{B-line upper and lower borders} = \frac{1}{2}W. \quad (16)$$

**Step 4.** Note that B-lines originate from the pleural line and should extend to the bottom of the ultrasound image, thus verification is needed to eliminate the Z-lines - these artefacts do not erase A-lines and have no use for diagnosis. Specifically, We discard the candidate B-lines that intersect with A-lines in the spatial domain, and the remaining ones are identified as the final detected B-lines.

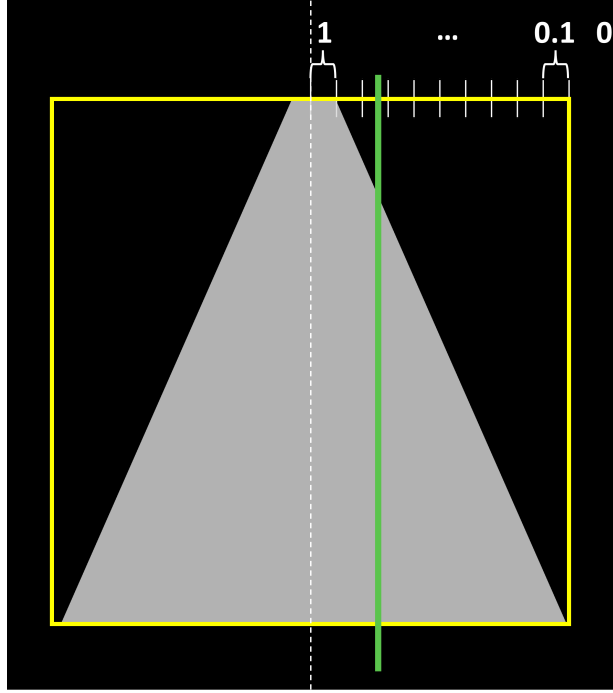


Fig. 4. An example of scoring the detected B-line. In this case, the green line is scored 0.8.

### III. SCORING RULES

To statistically evaluate the proposed method, we design rules for scoring the detected B-lines. As sketched in Fig. 4, the yellow bounding box (bbox) represents the ground truth where a B-line is located, and the green line indicates the location of detection. The width of the bbox is divided into ten regions on each side of a center line. The closer the green line is to the center line, the higher the score it receives, with scores ranging from 1 to 0.1 in decrements of 0.1 as the distance from the center line increases. Each region closest to the center line scores 1, decreasing by 0.1 for each subsequent region moving away from the center. Any green lines falling outside the bbox receive a score of 0, indicating no accuracy in detection within the target area. This scoring system provides a symmetrical and graded assessment of detection accuracy, offering precise feedback on the positioning of detections relative to the target area.

### IV. RESULTS AND DISCUSSION

#### A. Dataset

The video clips were obtained from 45 patients from the Nephrology, Dialysis and Transplantation Department, Careggi University Hospital, Florence, Italy. LUS evaluations were performed whilst patients attended for regular hemodialysis, using an ultrasound machine (MyLab Class C-Esaote®, Genoa, Italy) with a 6–18 MHz linear probe. The data was saved in DICOM format.

Data preprocessing includes extracting the frames from the video clips, cropping the region that only contains lung information, and finally padding all the images to the size of  $480 \times 600$  pixels (height  $\times$  width).

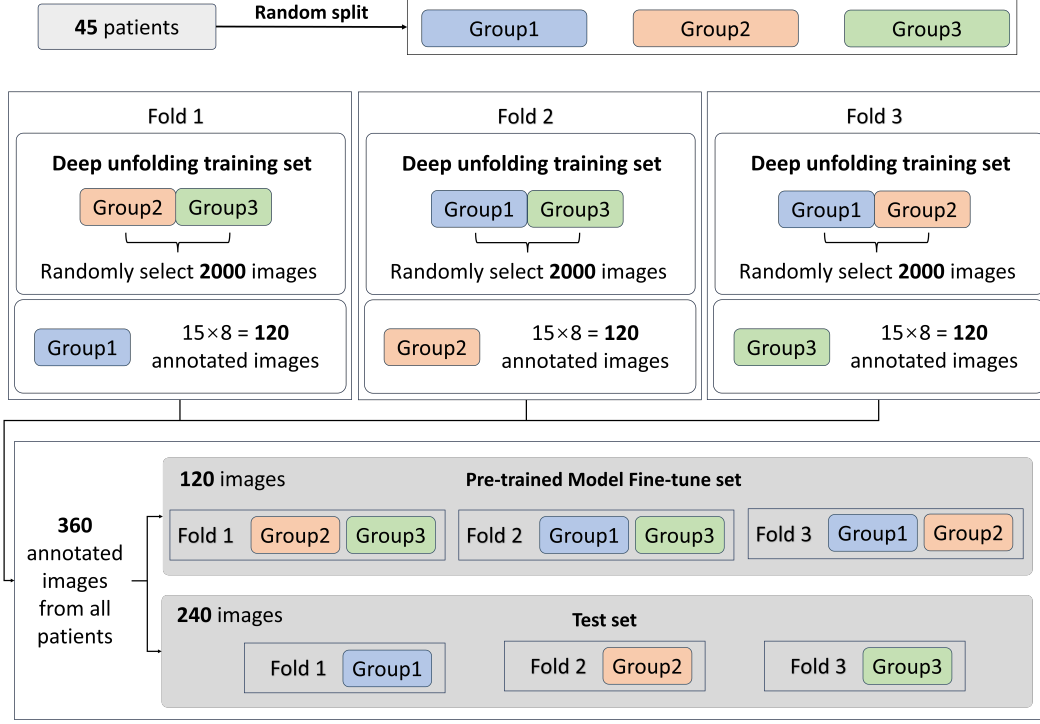


Fig. 5. Illustration of setting up the dataset. Data random splitting is implemented twice, each of which is designed to perform a 3-fold validation.

We randomly split the dataset into three groups (Group1, Group2, and Group3) at the patient level. Each of the groups contains data from 15 patients. By partitioning the dataset into 3 subsets, we will evaluate the proposed method in a 3-fold manner. This helps prevent information leakage between groups and iteratively uses each subset for testing while the remaining subsets are used for training. The training set in each fold is formed by randomly selecting 2000 images from two of the groups (for example Group1 and Group2). Then we randomly select 8 images from each patient in the remaining group (for example Group3), and a physician with long-term expertise in LUS provides the annotation of the line artefacts as the ground truth. The annotated images are subsequently divided into two sets which are used for pre-trained model (for example YOLOv7 [36] and FasterRCNN [37]) fine-tuning and algorithm testing respectively. The final test set contains in total 240 images. The detailed data splitting strategy is illustrated in Fig. 5. The procedure is implemented twice to enhance result stability and increase the reliability and credibility of the experiment by assessing consistency, minimizing chance influences, and aiding in issue identification.

### B. Experimental setup

We evaluated the B-line detection performance among several methods including PUI [9], CPS [12], DUBLINE [27], YOLOv7 [36] and FasterRCNN [37]. For model-based methods, we implement the experiment using MATLAB R2023a with 64-bit OS 12th Gen Intel® Core™ i7-12700 2.10 GHz. Regarding the deep unfolding technique, the networks are all implemented in PyTorch and are trained for 20 epochs on Nvidia Geforce RTX 3090. The number

of layers is set to 10 and 7 for DUBLINE and DUCPS respectively. The initial learning rate is set to  $10^{-4}$  for both methods and a scheduler is used to adjust the learning rate by 0.5 after 5 epochs. In the case of training with N2N loss, we set  $\alpha = 1$  as suggested in [34]. YOLOv7 and FasterRCNN are fine-tuned and then tested on the same GPU. It's important to note that while the networks are loaded onto the GPU for training, the computations related to the methods are performed on the same CPU setup utilized for model-based methods.

### C. Results Analysis

Our assessment is performed in terms of true positives (TP), false positives (FP), false negatives (FN), precision, recall, and the F-scores. We pay more attention to the F2 score as it is crucial to focus on minimizing FNs in medical contexts, where detecting all artefacts is paramount to prevent misdiagnoses and ensure timely treatment. Specifically, we use the threshold of 0.5 so as to calculate the values based on the scoring rules proposed in Section III. Detections that are scored above the threshold are counted as TP. For YOLOv7 and FasterRCNN, we summarised the results with the confidence threshold being 0.5. The statistical analysis is presented in Table I. Besides, we compared the performance of employing different line identification schemes (where the line identification method proposed in this paper is denoted as LIM) and different loss functions (SSIM and N2N).

By comparing the results of the original PUI algorithm and a version of it obtained by replacing the line identification part with LIM (referred to as PUI\_LIM thereafter), it can be demonstrated that our proposed line identification strategy improves overall detection performance when employing the same optimization techniques, particularly enhancing the recall with an average increase of 10.44% compared to [9].

Within the same line identification scheme, deep unfolding techniques have been instrumental in improving recall. Specifically, both DUBLINE\_SSIM+LIM and DUCPS\_SSIM+LIM, designed upon traditional optimization algorithms, have increased recall by 9.28% and 10.21% compared to PUI\_LIM and CPS+LIM respectively, consequently resulting in higher F2 scores. It is worth noting that the initial design of CPS was intended for handling curvilinear probe images. Although we adjusted parameters to adapt to the dataset in this study, CPS still exhibited low precision in the experiments. However, DUCPS enables the training of parameters within the optimization procedure, significantly enhancing the algorithm's generalization ability and boosting precision by 13.96%.

To find out the impact of different loss functions on experimental results, we can observe DUCPS\_SSIM+LIM and DUCPS\_N2N+LIM. Using the N2N loss led to the best performance across various matrices in model-based methods. While improving the average precision to 47.28%, it also raised recall to 70.13%. Additionally, both F1 and F2 scores reached their highest values among all methods, achieving 0.5633 and 0.6381, respectively. We also noticed that due to the sub-sampling technique utilized in the N2N loss, the network training requires less memory compared to using SSIM loss, resulting in faster training speeds.

Examining the performance of deep learning neural networks on the test data, we notice that while achieving relatively high scores in some folds, such as YOLOv7 reaching 100% precision in Fold 3 of the first random splitting, the proportion of FN is excessively high. A similar situation is observed in the testing of FasterRCNN in Random2-Fold2. In clinical settings, this could result in artefacts undetected, potentially causing patients to miss the window for treatment. Additionally, in some tests, neither YOLOv7 nor FasterRCNN predicted any artifacts with

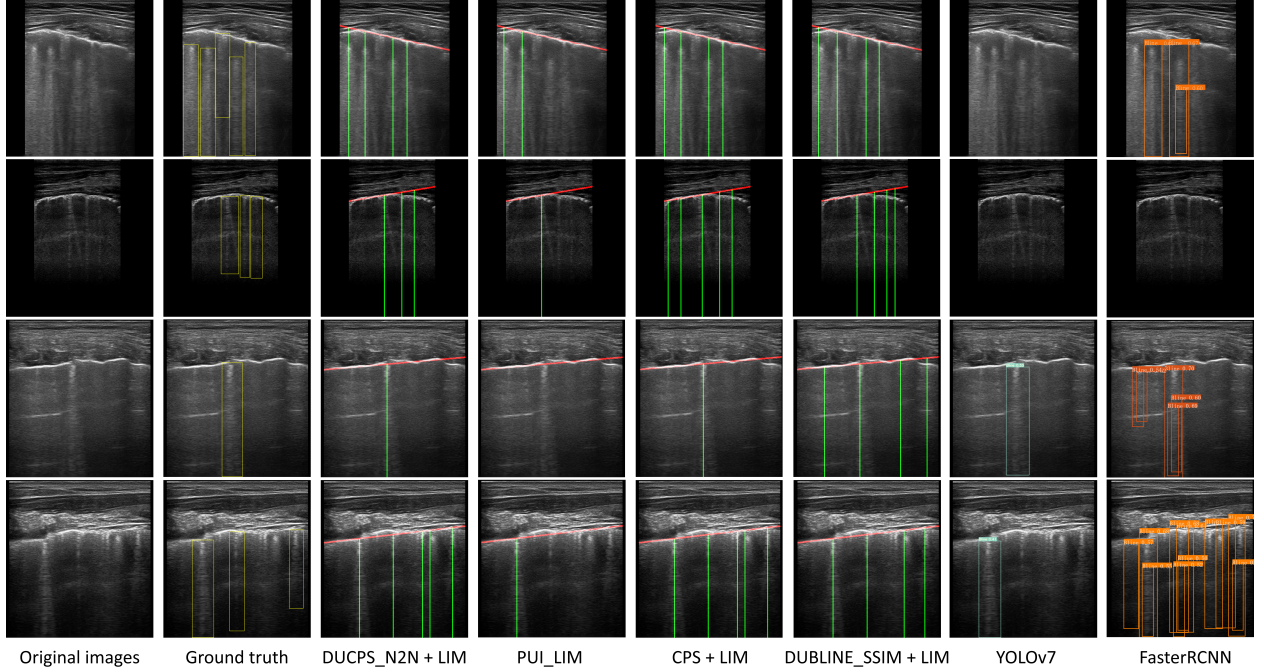


Fig. 6. Line detection results for various frames from different patients. Ground truth is annotated by yellow bounding boxes. For model-based methods and deep unfolding methods, pleural lines are depicted as red lines, and detected B-lines are shown as green lines. For YOLOv7 and FasterRCNN, detected B-lines are shown in blue and orange boxes, respectively.

confidence scores higher than 0.5. The same scenario occurred when testing other detection networks, including CascadeRCNN [38], CenterNet [39], DETR [40], and RetinaNet [41]. This may be due to the fine-tuning dataset being too small, leading the neural networks to not learn sufficient artefact features, highlighting the importance of dataset and annotation quality for deep learning neural networks. In contrast, DUCPS demonstrates robustness across all tests and does not require data annotation.

Fig. 6 shows the line artefact detection results for different methods. Through visualization of the results, we observe that compared to PUI\_LIM, our proposed approach reduces the probability of missed detections, thereby decreasing FNs, particularly in scenarios with high B-line density (as shown in row 1 and row 3). While CPS [12] and DUBLINE\_SSIM [27]+LIM also detect more B-lines, our method exhibits fewer FPs, as evident in row 2 and row 3. Compared to the detection results of deep learning neural networks, the stability of the proposed method is highlighted. For instance, YOLOv7 [36] often fails to confidently predict the presence of B-Lines in many instances (e.g., row 1, row 2, and row 3), while the results of FasterRCNN [37] show greater variability, ranging from failure to detect B-lines (row 2) to detecting excessive artifacts (row 4). Additionally, although there are accurate B-line localisations in some cases, there are frequent occurrences of overlapping predicted positions, and many predicted B-lines do not meet the condition of originating from the pleural line (row 1, row 3, and row 4). It is worth noting that the proposed method still has limited ability to distinguish genuine B-lines from some vertical artifacts, often misidentifying bright artifacts as B-lines, as shown in row 4.



TABLE I

LINE DETECTION PERFORMANCE (THRESHOLD = 0.5). DATA RANDOM SPLITTING IS EXECUTED TWICE, WITH EACH INSTANCE TAILORED FOR CONDUCTING A 3-FOLD VALIDATION. THE BEST AVERAGE PERFORMANCES ARE IN BOLD. THE BEST PERFORMANCE IN AN INDIVIDUAL FOLD IS INDICATED BY AN UNDERLINED ITALICS.

			Precision $\uparrow$	Recall $\uparrow$	F1 $\uparrow$	F2 $\uparrow$	Num_Bline	Num_Detection	TP $\uparrow$	FP $\downarrow$	FN $\downarrow$
PUI [9]	Random1	Fold1	0.53	0.47	0.50	0.49	99	88	47	41	52
		Fold2	0.52	0.53	0.52	0.53	109	112	58	54	51
		Fold3	0.34	0.42	0.38	0.40	85	106	36	70	49
	Random2	Fold1	0.52	0.49	0.51	0.50	136	128	67	61	69
		Fold2	0.49	0.44	0.47	0.45	91	81	40	41	51
		Fold3	0.35	0.52	0.42	0.47	66	97	34	63	32
	average		0.46	0.48	0.47	0.47					
PUI_LIM	Random1	Fold1	0.44	0.48	0.46	0.48	99	108	48	60	51
		Fold2	0.51	0.61	0.55	0.58	109	129	66	63	43
		Fold3	0.46	0.65	0.54	0.60	85	119	55	64	30
	Random2	Fold1	0.57	0.54	0.55	0.54	136	129	73	56	63
		Fold2	0.49	0.59	0.53	0.57	91	111	54	57	37
		Fold3	0.36	0.64	0.46	0.55	66	116	42	74	24
	average		0.47	0.58	0.52	0.55					
CPS [12]+LIM	Random1	Fold1	0.39	0.72	0.51	0.62	99	180	71	109	28
		Fold2	0.27	0.53	0.36	0.44	109	217	58	159	51
		Fold3	0.28	0.55	0.37	0.46	85	168	47	121	38
	Random2	Fold1	0.42	0.69	0.52	0.61	136	225	94	131	42
		Fold2	0.23	0.45	0.30	0.38	91	178	41	137	50
		Fold3	0.25	0.61	0.35	0.47	66	162	40	122	26
	average		0.31	0.59	0.40	0.50					
DUBLINE [27]_SSIM+LIM	Random1	Fold1	0.41	0.71	0.52	0.62	99	172	70	102	29
		Fold2	0.42	0.61	0.50	0.56	109	160	67	93	42
		Fold3	0.32	0.67	0.44	0.55	85	176	57	119	28
	Random2	Fold1	0.46	0.62	0.53	0.58	136	184	84	100	52
		Fold2	0.34	0.60	0.43	0.52	91	164	55	109	36
		Fold3	0.32	0.67	0.43	0.55	66	137	44	93	22
	average		0.38	0.65	0.47	0.56					
YOLOv7 [36]	Random1	Fold1	0.81	0.25	0.38	0.29	99	31	25	6	74
		Fold2	NaN	0.00	NaN	NaN	109	0	0	0	109
		Fold3	<u>1.00</u>	0.08	0.15	0.10	85	7	7	0	78
	Random2	Fold1	0.00	0.00	NaN	NaN	136	31	0	31	136
		Fold2	0.86	0.73	<u>0.79</u>	<u>0.75</u>	91	77	66	11	25
		Fold3	NaN	0.00	NaN	NaN	66	0	0	0	66
	average		<b>0.67</b>	0.27	0.33	0.29					
FasterRCNN [37]	Random1	Fold1	0.33	0.52	0.40	0.46	99	155	51	104	48
		Fold2	0.52	0.13	0.21	0.15	109	27	14	13	95
		Fold3	NaN	0.00	NaN	NaN	85	0	0	0	78
	Random2	Fold1	NaN	0.00	NaN	NaN	136	0	0	0	136
		Fold2	0.94	0.33	0.49	0.38	91	32	30	2	61
		Fold3	NaN	0.00	NaN	NaN	66	0	0	0	66
	average		0.60	0.32	0.37	0.33					
DUCPS_SSIM+LIM (ours)	Random1	Fold1	0.47	0.71	0.56	0.64	99	149	70	79	29
		Fold2	0.49	0.68	0.57	0.63	109	152	74	78	35
		Fold3	0.40	0.71	0.51	0.61	85	151	60	91	25
	Random2	Fold1	0.54	0.76	0.63	0.70	136	191	103	88	33
		Fold2	0.41	0.57	0.48	0.53	91	126	52	74	39
		Fold3	0.37	0.74	0.49	0.62	66	133	49	84	17
	average		0.45	0.69	0.54	0.62					
DUCPS_N2N+LIM (ours)	Random1	Fold1	0.51	<u>0.78</u>	0.62	0.70	99	151	77	74	22
		Fold2	0.51	0.65	0.57	0.62	109	139	71	68	38
		Fold3	0.42	0.68	0.52	0.61	85	138	58	80	27
	Random2	Fold1	0.56	0.76	0.65	0.71	136	186	104	82	32
		Fold2	0.42	0.60	0.50	0.56	91	130	55	75	36
		Fold3	0.41	0.73	0.53	0.63	66	116	48	68	18
	average		0.47	<b>0.70</b>	<b>0.56</b>	<b>0.64</b>					

TABLE II  
AVERAGE OPTIMIZATION SPEED ON THE TEST SET (SECONDS/FRAME).

CPU only	PUI [9]*	CPS [12]**	DUBLINE_SSIM [27]	DUCPS_SSIM	DUCPS_N2N
	4.1443	1.3239	15.4906	15.8665	15.9449
GPU	YOLOv7 [36]	FasterRCNN [37]	DUBLINE_SSIM [27]	DUCPS_SSIM	DUCPS_N2N
	0.0423	0.0924	0.1079	0.1194	0.2542

\* Excluding the line identification part.

\*\* Excluding data that exceeds the maximum iteration count.

Table II illustrates the average runtime of different optimization methods on the test dataset. Although deep unfolding methods run slowly utilizing CPU only, it is evident that employing deep unfolding significantly enhances algorithmic optimization efficiency with the assistance of GPU. When trained with SSIM loss, DUBLINE\_SSIM and DUCPS\_SSIM exhibit runtimes of 0.1079 seconds/frame and 0.1194 seconds/frame, respectively, representing an efficiency improvement of at least 30 times compared to PUI [9]. It is worth noting that in CPS [12], situations may arise where the iteration count exceeds the maximum without convergence; such cases are not included in the statistical results presented in the table. Nevertheless, the execution speed of deep unfolding surpasses CPS by over tenfold. With N2N loss, although the optimization time slightly increases due to the higher complexity of the loss function compared to SSIM, the processing speed per frame still remains below 1 second.

## V. CONCLUSION

The detection of artefacts in LUS, particularly B-lines, is gaining increasing attention in clinical practice due to their significant diagnostic value. In this work, we introduce a novel and explainable framework called DUCPS for B-line detection, leveraging the technique of deep unfolding to combine the strengths of traditional model-based methods and deep learning approaches. By unfolding the CPS into a multi-layer network, the parameters in the optimization algorithm become learnable, improving the algorithm's generalization performance and achieving rapid convergence. Subsequently, we train the network in a totally unsupervised manner, achieving the best performance across all metrics when using the N2N loss function. When utilizing the SSIM loss function, the algorithm exhibits the highest optimization efficiency. Overall, the proposed method enhances the computational efficiency of traditional algorithms while achieving robust detection without the need for extensive data labeling.

The limitation of this work stems from its relatively low precision. While high recall effectively avoids missed detections, the increased FPs can contribute to the workload of repeated validation in clinical diagnosis, which is an aspect requiring further attention in future work.

## REFERENCES

- [1] T. Yang, O. Karakuş, N. Anantrasirichai, and A. Achim, "Current advances in computational lung ultrasound imaging: a review," *IEEE Transactions on Ultrasonics, Ferroelectrics, and Frequency Control*, 2022.
- [2] D. A. Lichtenstein, "Lung ultrasound in the critically ill," *Annals of Intensive Care*, vol. 4, no. 1, pp. 1–12, 2014.
- [3] V. E. Noble, A. F. Murray, R. Capp, M. H. Sylvia-Reardon, D. J. Steele, and A. Liteplo, "Ultrasound assessment for extravascular lung water in patients undergoing hemodialysis: time course for resolution," *Chest*, vol. 135, no. 6, pp. 1433–1439, 2009.

- [4] M. Allinovi, M. Saleem, P. Romagnani, P. Nazerian, and W. Hayes, "Lung ultrasound: a novel technique for detecting fluid overload in children on dialysis," *Nephrology Dialysis Transplantation*, vol. 32, no. 3, pp. 541–547, 2017.
- [5] Q. Fu, Z. Chen, J. Fan, C. Ling, X. Wang, X. Liu, and Y. Shen, "Lung ultrasound methods for assessing fluid volume change and monitoring dry weight in pediatric hemodialysis patients," *Pediatric Nephrology*, vol. 36, no. 4, pp. 969–976, 2021.
- [6] L. J. Brattain, B. A. Telfer, A. S. Liteplo, and V. E. Noble, "Automated B-line scoring on thoracic sonography," *Journal of Ultrasound in Medicine*, vol. 32, no. 12, pp. 2185–2190, 2013.
- [7] R. Moshavegh, K. L. Hansen, H. Møller-Sørensen, M. B. Nielsen, and J. A. Jensen, "Automatic detection of B-lines in *in vivo* lung ultrasound," *IEEE Transactions on Ultrasonics, Ferroelectrics, and Frequency Control*, vol. 66, no. 2, pp. 309–317, 2019.
- [8] N. Anantrasirichai, M. Allinovi, W. Hayes, and A. Achim, "Automatic B-line detection in paediatric lung ultrasound," in *2016 IEEE International Ultrasonics Symposium (IUS)*. IEEE, 2016, pp. 1–4.
- [9] N. Anantrasirichai, W. Hayes, M. Allinovi, D. Bull, and A. Achim, "Line detection as an inverse problem: application to lung ultrasound imaging," *IEEE Transactions on Medical Imaging*, vol. 36, no. 10, pp. 2045–2056, 2017.
- [10] S. Boyd, N. Parikh, E. Chu, B. Peleato, J. Eckstein *et al.*, "Distributed optimization and statistical learning via the alternating direction method of multipliers," *Foundations and Trends® in Machine learning*, vol. 3, no. 1, pp. 1–122, 2011.
- [11] M. Farahi, J. Aranda, H. Habibian, and A. Casals, "Automatic feature detection in lung ultrasound images using wavelet and radon transforms," *arXiv preprint arXiv:2306.12780*, 2023.
- [12] O. Karakuş, N. Anantrasirichai, A. Aguersif, S. Silva, A. Basarab, and A. Achim, "Detection of line artifacts in lung ultrasound images of COVID-19 patients via nonconvex regularization," *IEEE Transactions on Ultrasonics, Ferroelectrics, and Frequency Control*, pp. 2218–2229, 2020.
- [13] O. Karakuş, P. Mayo, and A. Achim, "Convergence guarantees for non-convex optimisation with Cauchy-based penalties," *IEEE Transactions on Signal Processing*, vol. 68, pp. 6159–6170, 2020.
- [14] R. J. Van Sloun and L. Demi, "Localizing B-lines in lung ultrasonography by weakly supervised deep learning, in-vivo results," *IEEE Journal of Biomedical and Health Informatics*, pp. 957–964, 2019.
- [15] R. R. Selvaraju, M. Cogswell, A. Das, R. Vedantam, D. Parikh, and D. Batra, "Grad-CAM: Visual explanations from deep networks via gradient-based localization," in *Proceedings of the IEEE International Conference on Computer Vision (ICCV)*, 2017, pp. 618–626.
- [16] S. Roy, W. Menapace, S. Oei, B. Luijten, E. Fini, C. Saltori, I. Huijben, N. Chennakeshava, F. Mento, A. Sentelli, E. Peschiera, R. Trevisan, G. Maschietto, E. Torri, R. Inchingolo, A. Smargiassi, G. Soldati, P. Rota, A. Passerini, R. J. G. van Sloun, E. Ricci, and L. Demi, "Deep learning for classification and localization of COVID-19 markers in point-of-care lung ultrasound," *IEEE Transactions on Medical Imaging*, vol. 39, no. 8, pp. 2676–2687, 2020.
- [17] O. Frank, N. Schipper, M. Vaturi, G. Soldati, A. Smargiassi, R. Inchingolo, E. Torri, T. Perrone, F. Mento, L. Demi, M. Galun, Y. C. Eldar, and S. Bagon, "Integrating domain knowledge into deep networks for lung ultrasound with applications to COVID-19," *IEEE Transactions on Medical Imaging*, vol. 41, no. 3, pp. 571–581, 2021.
- [18] C. Baloesu, G. Toporek, S. Kim, K. McNamara, R. Liu, M. M. Shaw, R. L. McNamara, B. I. Raju, and C. L. Moore, "Automated lung ultrasound B-line assessment using a deep learning algorithm," *IEEE Transactions on Ultrasonics, Ferroelectrics, and Frequency Control*, pp. 2312–2320, 2020.
- [19] H. Kerdegari, N. T. H. Phung, A. McBride, L. Pisani, H. V. Nguyen, T. B. Duong, R. Razavi, L. Thwaites, S. Yacoub, A. Gomez, and V. Consortium, "B-line detection and localization in lung ultrasound videos using spatiotemporal attention," *Applied Sciences*, p. 11697, 2021.
- [20] L. Zhao, T. C. Fong, and M. A. L. Bell, "COVID-19 feature detection with deep neural networks trained on simulated lung ultrasound B-mode images," in *2022 IEEE International Ultrasonics Symposium (IUS)*. IEEE, 2022, pp. 1–3.
- [21] T. Yang, N. Anantrasirichai, O. Karakuş, M. Allinovi, and A. Achim, "A semi-supervised learning approach for B-line detection in lung ultrasound images," *2023 IEEE 20th International Symposium on Biomedical Imaging (ISBI)*, pp. 1–5, 2022.
- [22] K. Gregor and Y. LeCun, "Learning fast approximations of sparse coding," in *Proceedings of the 27th International Conference on International Conference on Machine Learning*, 2010.
- [23] Y. Yang, J. Sun, H. Li, and Z. Xu, "ADMM-CSNet: A deep learning approach for image compressive sensing," *IEEE Transactions on Pattern Analysis and Machine Intelligence*, vol. 42, no. 3, pp. 521–538, 2018.
- [24] J. Adler and O. Öktem, "Learned Primal-Dual reconstruction," *IEEE Transactions on Medical Imaging*, vol. 37, no. 6, pp. 1322–1332, 2018.

- [25] E. Kang, W. Chang, J. Yoo, and J. C. Ye, "Deep convolutional framelet denosing for low-dose CT via wavelet residual network," *IEEE Transactions on Medical Imaging*, vol. 37, no. 6, pp. 1358–1369, 2018.
- [26] R. J. Van Sloun, R. Cohen, and Y. C. Eldar, "Deep learning in ultrasound imaging," *Proceedings of the IEEE*, vol. 108, no. 1, pp. 11–29, 2019.
- [27] T. Yang, N. Anantrasirichai, O. Karakuş, M. Allinovi, H. C. Koydemir, and A. Achim, "DUBLINE: A deep unfolding network for b-line detection in lung ultrasound images," *arXiv preprint arXiv:2311.06672*, 2023.
- [28] B. T. Kelley and V. K. Madisetti, "The fast discrete radon transform. i. theory," *IEEE Transactions on Image Processing*, vol. 2, no. 3, pp. 382–400, 1993.
- [29] A. Achim and E. E. Kuruoglu, "Image denoising using bivariate  $\alpha$ -stable distributions in the complex wavelet domain," *IEEE Signal Proc. Letters*, vol. 12, pp. 17–20, Jan. 2005.
- [30] A. Achim, A. Bezerianos, and P. Tsakalides, "Novel Bayesian multiscale method for speckle removal in medical ultrasound images," *IEEE Trans. Med. Imag.*, vol. 20, pp. 772–783, Aug. 2001.
- [31] A. Balatsoukas-Stimming and C. Studer, "Deep unfolding for communications systems: A survey and some new directions," in *2019 IEEE International Workshop on Signal Processing Systems (SiPS)*, 2019, pp. 266–271.
- [32] L. Z. Gengsheng, *Medical Image Reconstruction: A Conceptual Tutorial*. Higher Education Press, 2010.
- [33] A. Loza, D. Bull, N. Canagarajah, and A. Achim, "Non-Gaussian model-based fusion of noisy images in the wavelet domain," *Computer Vision and Image Understanding*, vol. 114, no. 1, pp. 54–65, 2010.
- [34] T. Huang, S. Li, X. Jia, H. Lu, and J. Liu, "Neighbor2Neighbor: Self-supervised denoising from single noisy images," in *Proceedings of the IEEE/CVF Conference on Computer Vision and Pattern Recognition (CVPR)*, 2021, pp. 14 781–14 790.
- [35] Z. Wang, A. C. Bovik, H. R. Sheikh, and E. P. Simoncelli, "Image quality assessment: from error visibility to structural similarity," *IEEE Transactions on Image Processing*, pp. 600–612, 2004.
- [36] C.-Y. Wang, A. Bochkovskiy, and H.-Y. M. Liao, "YOLOv7: Trainable bag-of-freebies sets new state-of-the-art for real-time object detectors," in *Proceedings of the IEEE/CVF Conference on Computer Vision and Pattern Recognition (CVPR)*, 2023, pp. 7464–7475.
- [37] S. Ren, K. He, R. Girshick, and J. Sun, "Faster R-CNN: Towards real-time object detection with region proposal networks," *Advances in Neural Information Processing Systems*, vol. 28, 2015.
- [38] Z. Cai and N. Vasconcelos, "Cascade R-CNN: Delving into high quality object detection," in *2018 IEEE/CVF Conference on Computer Vision and Pattern Recognition (CVPR)*, 2018, pp. 6154–6162.
- [39] K. Duan, S. Bai, L. Xie, H. Qi, Q. Huang, and Q. Tian, "CenterNet: Keypoint triplets for object detection," in *2019 IEEE/CVF International Conference on Computer Vision (ICCV)*, 2019, pp. 6568–6577.
- [40] N. Carion, F. Massa, G. Synnaeve, N. Usunier, A. Kirillov, and S. Zagoruyko, "End-to-end object detection with transformers," in *European Conference on Computer Vision (ECCV)*. Springer, 2020, pp. 213–229.
- [41] T.-Y. Lin, P. Goyal, R. Girshick, K. He, and P. Dollar, "Focal loss for dense object detection," in *Proceedings of the IEEE International Conference on Computer Vision (ICCV)*, Oct 2017.